Chapter 11

Muon Geotomography—Bringing New Physics to Orebody Imaging

Douglas Bryman,[1,†] James Bueno,[2] Kris Davis,[3] Vlad Kaminski,[3] Zhiyi Liu,[2] Douglas Oldenburg,[3]
Mark Pilkington,[4] and Richard Sawyer[5]

[1] *Department of Physics and Astronomy, University of British Columbia, 6224 Agricultural Road,
Vancouver, British Columbia V6T 1Z1, Canada*

[2] *Advanced Applied Physics Solutions, 4004 Wesbrook Mall, Vancouver, British Columbia V6T 2A3, Canada*

[3] *Geophysical Inversion Facility, Department of Earth and Ocean Sciences, University of British Columbia,
2020-2207 Main Mall, Vancouver, British Columbia V6T 1Z4, Canada*

[4] *Geological Survey of Canada, Central Canada Division, 615 Booth Street, Ottawa, Ontario K1A 0E9, Canada*

[5] *Nyrstar Myra Falls, P.O. Box 8000, Campbell River, British Columbia V9W 5E2, Canada*

Abstract

Muon geotomography, a novel geophysical exploration and imaging technology, uses cosmic rays to create three-dimensional (3-D) images of subsurface density distributions. The first controlled field test confirming the capability of muon geotomography for imaging a dense orebody in a complex geologic environment was conducted at the Price volcanic-hosted massive sulfide (VHMS) deposit, Vancouver Island, British Columbia, Canada. The semimassive and massive polymetallic mineralization of the Price deposit is situated in a Paleozoic stratigraphic package of rocks known as the Sicker Group including the Price, Myra, Thelwood, and Flower Ridge Formations, indicative of volcanic rocks formed in a rifted oceanic island-arc system. The field application involved placing a sensor with an active area of 1 m² beneath the massive sulfide orebody in an underground tunnel for exposures of about two weeks at several locations. Muon flux data were inverted to recover a 3-D density image of the deposit. The inverted data were in good agreement with drill core data. However, some distortions of the image were observed due to the limitations imposed by the available tunnel which restricted the angular views available to the sensors. Muon geotomography works best when sensors are placed such that they can view the region under study from a range of different angles. The demonstrated ability to perform accurate forward model simulations makes the sensitivity of the technique predictable for specific survey situations. The results demonstrate the potential of muon geotomography for identification and characterization of orebodies located in complex geologic environments. Three-dimensional images from muon geotomography surveys may be used to guide drilling operations toward regions of high-density contrast, thereby significantly reducing costs and environmental impact associated with locating orebodies.

Introduction

Electromagnetic, gravimetric, magnetic, and seismic surveys are routinely used for subsurface exploration and imaging of orebodies. We have developed a complementary technique, muon geotomography, which determines subsurface density by measuring the flux of naturally occurring cosmic ray muon particles at underground locations.

Muon geotomography, which uses the attenuation of cosmic ray muons in matter, is similar in principle to computed tomography scanning, but employs a naturally occurring source of radiation. High-energy protons from astrophysical sources interact in the Earth's atmosphere to produce pions and kaons, which are unstable elementary particles. These rapidly decay into various particles including muons, which are similar to electrons but are 200 times heavier. Although muons are also unstable particles, some are sufficiently energetic to reach the Earth's surface and penetrate up to several kilometers below ground.

At sea level the cosmic ray muon flux is 1 cm⁻² min⁻¹, with well-known angular and energy distributions (Beringer et al., 2012). Once below ground, high-energy cosmic ray muons follow relatively straight line trajectories as they slow down and stop; a typical angular deviation from a straight line trajectory is 10 mrad. Penetration depth depends on the muon's initial energy and the average density of material traversed. If the muons pass through denser mineralized zones than the surrounding rock, their survival rate is reduced by attenuation.

Muon count rates and trajectories can be monitored using common methods in particle physics, and from these count rates the integrated mass density between the sensor and the surface is determined for a complete range of trajectory directions. The data from several muon sensors form the input to a solvable inverse problem which yields a 3-D image of subsurface density. Geologic features can then be imaged with the resolution dependent on the exposure time, the depth of the sensors beneath the surface, the relative location of the muon sensors, and the quality of the topographic data.

An early use of cosmic ray muons for geologic applications was reported by George (1955), who measured rock thickness above a tunnel. Alvarez et al. (1970), working near the surface, ruled out hidden chambers in the Second Pyramid of Giza by measuring cosmic ray muon attenuation. More recently, cosmic ray muon imaging has been applied in determining

† Corresponding author: e-mail, doug@triumf.ca

density distributions in volcanoes (Tanaka et al., 2011, and references therein).

In the present study, conventional geophysical inversion techniques (e.g., Oldenburg and Li, 2005) were applied to muon attenuation data. We report the results from a muon geotomography field trial at the Price volcanic-hosted massive sulfide (VHMS) deposit on Vancouver Island, British Columbia, Canada, and compare the inversion of field data with a model derived from drill core data.

Simulating Muon Tomographic Data

An essential aspect of muon geotomography involves conversion of muon fluxes to integrated mass density and vice versa. This is needed for the interpretation of field data and to develop synthetic data used for testing inversion algorithms.

In our work, muon fluxes at subsurface locations are simulated using a forward modeling code. At each sensor location the code calculates an expected muon flux and the integrated mass density between the sensor and surface. These calculations are carried out for discrete solid angles that cover the angular acceptance of each sensor. Using the expected muon flux, realistic uncertainties are calculated for the integrated mass density.

Calculation of the underground cosmic ray muon flux requires knowledge of it at the surface and an energy loss model for muons passing through the earth. In this study we use an empirical formula for the muon energy and angular spectrum at the surface (Tang et al., 2006), and the relationship between muon energy and depth is calculated with energy loss tables (Groom et al., 2001). Muon trajectories are assumed to be straight lines unaffected by multiple Coulomb scattering, the effect of which is negligible for our purposes. The integrated mass density can be converted to a length scale in meters if a background density is assumed. Figure 1 shows the calculated depth-intensity relationship for rock with density 2.7 g/cm^3 for three different zenith angles. For a more detailed discussion of underground cosmic ray muon flux, see Grieder (2001).
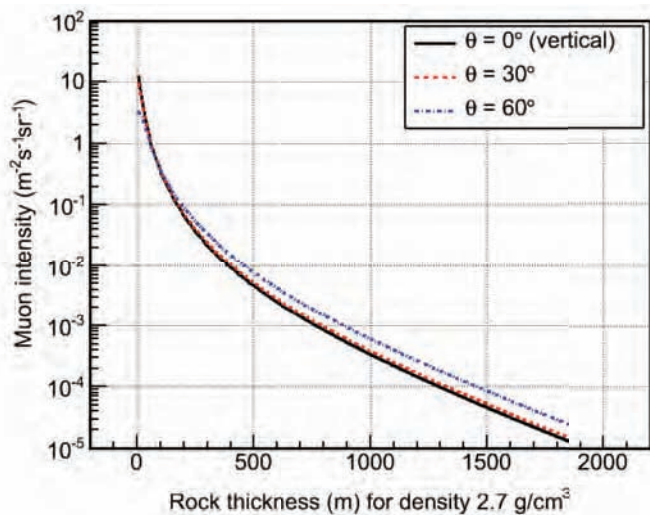

FIG. 1. Calculated cosmic ray muon intensity (m^{-2}s^{-1}sr^{-1}) vs. depth (m) for rock with density of 2.7 g/cm^3 for three zenith angles, derived from Tang et al. (2006) and Groom et al. (2001).

For each underground sensor, the forward modeling code calculates the integrated mass density between the sensor and surface, d, using

$$d(\theta, \phi) = \int_\Omega \rho(\ell,\theta,\phi)d\ell, \qquad (1)$$

where θ is the zenith angle, ϕ is the azimuth angle, Ω is a solid angle cone, $d\ell$ is a length element, and $\rho(\ell,\theta,\phi)$ is the subsurface density model. The integrated mass density, d, is converted into muon flux using the depth-intensity relationship in Figure 1, and from this flux the muon rate based on the sensor area is calculated. The muon rate multiplied by time gives the number of counts, N, which is assumed to follow a Poisson distribution with parameter N, giving an uncertainty of $\pm \sqrt{N}$. The two values $N \pm \sqrt{N}$ are then converted back into d_+ and d_-, and the uncertainty δ_d is set to the average of (d_+-d_-). Although the integrated mass density uncertainties are asymmetric, for the present purposes using symmetric values was satisfactory; the main concern is to obtain a reasonable estimate of the uncertainty of each datum and a good relative estimate of the errors on different data. Finally the integrated mass density central value is obtained by sampling from a Gaussian distribution with mean d and standard deviation equal to δ_d. The uncertainty, δ_d, is reduced by operating at shallower depths, extending the measurement duration, and increasing the sensor's sensitive area.

Inversion Methodology

In our mathematical representation, the earth volume has an upper surface that was determined by the topography and extended to depth below the sensors. We discretize the volume into M cuboidal cells each having a constant density. The relationship between the M densities $\boldsymbol{\rho}$ and the N data $\mathbf{d}$ (i.e., eq 1) is discretized as

$$\mathbf{d} = \mathbf{A}\boldsymbol{\rho}, \qquad (2)$$

where each element of $\mathbf{A}$, a_{ij}, is the length of ray i ($i = 1,...,N$) passing through cell j ($j = 1,...,M$) and ρ_j is the density of the cell. With a limited number of sensors and the grouping of all possible ray paths into averages, most cells are not crossed or sampled by any rays; this results in $\mathbf{A}$ being a sparse matrix containing only a few nonzero elements. The percentage of nonzero elements can be small. It is generally in the 0.01 to 0.1% range for the simulated and real cases discussed below.

For muon geotomography problems, the number of cells is usually much larger than the number of data leading to an underdetermined problem that does not have a unique solution. Some constraining or a priori information is therefore required to reduce this nonuniqueness. In this study we solve the linear inverse problem by minimizing a global objective function of the form,

$$\phi = \phi_d + \beta\phi_m, \qquad (3)$$

given the data constraints in equation (2) (Tikhonov and Arsenin, 1977; Menke, 1989; Parker, 1994; Oldenburg and Li, 2005), and where ϕ_d is a weighted data misfit function,

$$\varphi_d = (\boldsymbol{d} - \mathbf{A}\boldsymbol{\rho})^T \mathbf{D}(\boldsymbol{d} - \mathbf{A}\boldsymbol{\rho}). \qquad (4)$$

The data misfit function ensures that differences between the observed and calculated data are minimized in a least-squares sense. $\boldsymbol{D}$ is a diagonal weighting matrix with terms

$1/\sigma_i$, where σ_i is the estimated data error variance for the ith datum. Hence, the ray paths associated with large estimated errors contribute weakly to the solution. The model objective function, ϕ_m, is given as

$$\phi_m = (\boldsymbol{\rho} - \boldsymbol{\rho_0})^T \, \mathbf{P}(\boldsymbol{\rho} - \boldsymbol{\rho_0}), \tag{5}$$

where $\mathbf{P}$ is an $M \times M$ matrix given by

$$\mathbf{P} = \alpha_s \, \mathbf{W}_s^T \mathbf{W}_s + \alpha_x \, \mathbf{W}_x^T \mathbf{W}_x + \alpha_y \, \mathbf{W}_y^T \mathbf{W}_y + \alpha_z \, \mathbf{W}_z^T \mathbf{W}_z. \tag{6}$$

The model objective function stabilizes the solution in two ways. First, it keeps the calculated solution $\boldsymbol{\rho}$ close to some known density distribution $\boldsymbol{\rho_0}$, called the prior or reference model. If no prior geologic or density information is known, $\boldsymbol{\rho_0}$ is set to the best estimate of the host-rock density. Second, the model objective function (ϕ_m) is characterized by the matrix $\mathbf{P}$, and the structure of $\mathbf{P}$ can be altered to ensure certain spatial characteristics of the solution $\boldsymbol{\rho_0}$. In its simplest form, $\mathbf{P} = \mathbf{I}$, where $\mathbf{I}$ is the identity matrix, and the model objective function minimizes the variation in the solution, preventing or damping unwanted and unrealistic oscillatory behavior in $\boldsymbol{\rho_0}$. We generally use a stronger constraint on $\boldsymbol{\rho_0}$ by minimizing its closeness to the reference model through a volume-based weighting matrix of $\mathbf{W}_s$ as well as its roughness as defined by the spatial derivatives of the density distribution in the x, y, and z directions (i.e., $\mathbf{W}_x$, $\mathbf{W}_y$, and $\mathbf{W}_z$). Additional weights can be added by adjusting the value of α_s, α_x, α_y, and α_z to emphasize closeness to the reference model (α_s) or the smoothness in the x, y, or z directions.

The value of β, the trade-off between minimizing the misfit and minimizing the model objective function, can be chosen in a variety of ways. It can be assigned by trial and error, by successively reducing its value until the ϕ_d term reaches a target value, using an L-curve criterion (Hansen, 2000), or implementing a generalized cross-validation method (Golub et al., 1979).

Solving equation (3) results in a discretized model of the subsurface density distribution, $\boldsymbol{\rho}$. Because the inverse problem is linear in $\boldsymbol{\rho}$ we can also work with an anomalous density value $\boldsymbol{\rho_a}$ defined as

$$\boldsymbol{\rho_a} = \boldsymbol{\rho} - \boldsymbol{\rho_b}, \tag{7}$$

where $\boldsymbol{\rho_b}$ is an estimated density model for the host rock. Anomalous integrated mass density data are then given as

$$\mathbf{d}_a = \mathbf{A}(\boldsymbol{\rho} - \boldsymbol{\rho_b}) = \mathbf{A} \, \boldsymbol{\rho_a}. \tag{8}$$

When solving for anomalous density values, the total objective function and inversion methodology remains the same, except that the reference model $\boldsymbol{\rho_0}$ is set to zero and the observed data are the anomalous integrated mass density. The inversions described later in this paper used the anomalous density.

Field Application

Location and geologic setting

A muon geotomography proof-of-principle trial was conducted at the Nyrstar Myra Falls mining operation on Vancouver Island, British Columbia, Canada. This mine extracts zinc, copper, lead, silver, and gold from VHMS deposits. We chose to survey the Price deposit, which is a zinc-rich VHMS

deposit within the upper mineralized horizon of the Myra Formation, because it is relatively close to the surface, drill core data exists, and there were accessible tunnels suitably positioned to place muon sensors at locations below and adjacent to the ore. A cross section of the mine area is shown in Figure 2.

The Price deposit is situated in a Paleozoic group of rocks known as the Sicker Group including the Price, Myra, Thelwood, and Flower Ridge Formations indicative of volcanic rocks formed in a rifted oceanic island-arc system (Muller, 1980; Juras, 1987; Hamilton, 1995). The Price Formation consists of feldspar-pyroxene porphyritic basaltic andesite, mafic flow breccias, and coarse-grained volcaniclastic rocks that may be moderately to strongly epidote-chlorite-albite altered. The Myra Formation is composed of andesitic to rhyolitic flows and pyroclastic deposits, volcanic sediments, and hydrothermal sulfide mineralization related to the magmatic arc assemblage and intraback-arc rifting. The semimassive and massive polymetallic mineralization of the Price deposit is confined to this horizon. The Price and Myra Formations are unconformably overlain by rocks of the Thelwood and Flower Ridge Formations. The Thelwood Formation comprises mainly fine-grained siliceous tuffaceous sediments and subaqueous
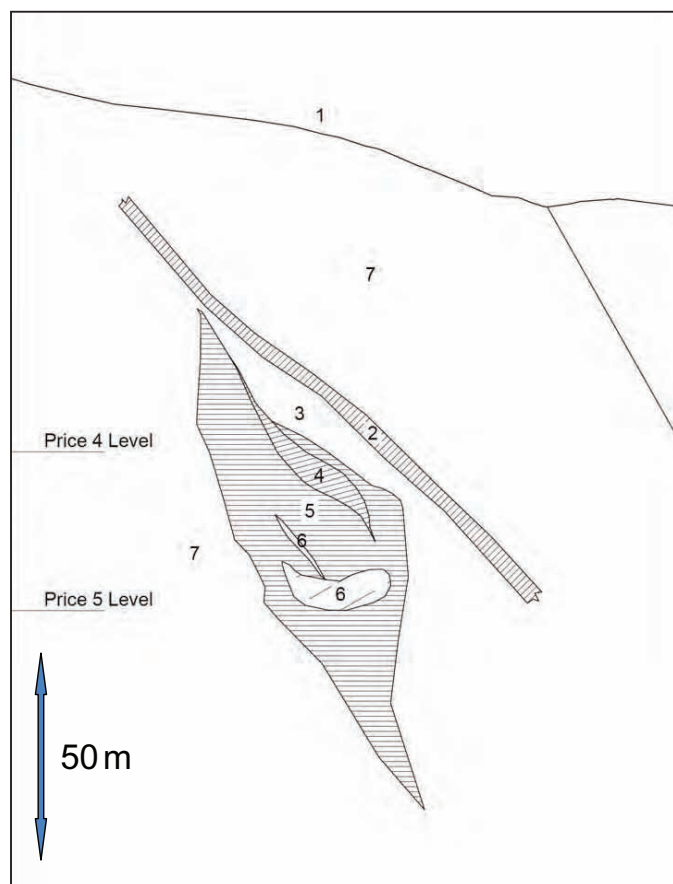

FIG. 2. Cross section schematic of the Price deposit region (see Juras, 1987). Geologic features illustrated are (1) bedrock topography, (2) hangingwall fault, (3) altered andesite volcaniclastic, (4) Price deposit, polymetallic sulfide orebody, (5) rhyolite intrusion, (6) altered country rock, and, (7) dacitice volcaniclastic rocks. The muon geotomography sensors were placed in an adit at the Price 5 level located beneath the deposit.

pyroclastic and volcaniclastic debris flows. The Flower Ridge Formation conformably overlies the Thelwood Formation and consists of amygdaloidal feldspar-pyroxene porphyritic basaltic lapilli tuff as well as pyroclastic breccia and tuffaceous sediments.

The deposit is located at an elevation of about 600 m above sea level and the densest part is 66 m below surface level. The orebody is >500 m in length and had been delineated using 225 diamond drill holes at 15- to 30-m intervals. These core samples were used to create a geologic block model of the deposit. Figure 3 shows the anomalous density from this model, which was derived as follows: density values were extracted from drill core assays, and these values were put into continuous 4-m composite intervals. Data points were then derived from a search ellipse extrapolated on an inverse distance cubed basis along x, y, and z axis lengths of 50, 30, and 15 m, respectively, with a block size of $2.5 \times 2.5 \times 2.5$ m. Anything outside of the ore outline was assigned a default value of 2.7 g/cm³. The resulting model had a median (maximum) deposit density of 3.0 g/cm³ (4.6 g/cm³), and the maximum thickness of the mineralization was about 15 m.

The region's topography is mountainous with thick tree cover. Over the survey region, the surface elevation varies between 651 and 938 m above sea level. Topography data from an airborne LIDAR survey was used to extract a bare-earth model with an estimated elevation accuracy of 1 m. The LIDAR survey was consistent with a less accurate British Columbia Geographic Map (TRIM).

Muon sensor

The muon tracking sensor (Fig. 4), based on detector designs used in the MINERνA experiment (MINERνA collaboration, 2006), had an active area of 1 m². Muon trajectories were reconstructed with angular resolution <0.6°, up to a maximum zenith angle of 60°. Laboratory tests showed that the detection efficiency exceeded 99% for vertical trajectories.

Data acquisition

The sensor was transported by truck from Vancouver to the Myra Falls mine, and then by helicopter to the entrance of the Price 5 mine tunnel. Before entering the tunnel, the sensor was operated on the surface to ensure its functionality after

FIG. 4. Muon sensor enclosure on a rail cart prior to entry into the mine tunnel.

transportation, and measurements were checked against the expected cosmic ray muon flux.

The sensor was then placed at seven underground locations shown in Figure 5. Sites labeled B1 to B6 were separated by about 30 m and site A1 was closer to the mine entrance. These locations maximized the angular coverage of the deposit as determined by simulations of the drill core data. The exposure times for sites B1 to B5 and A1 were about two weeks, yielding 1.5×10^5 muons per site. One site, B6, had a 43-week exposure time yielding 3×10^6 muons. Each measurement location was surveyed for sensor position and orientation.

Results and discussion

Data from the B6 location are compared to the predicted muon counts in Figure 6. The measured counts were
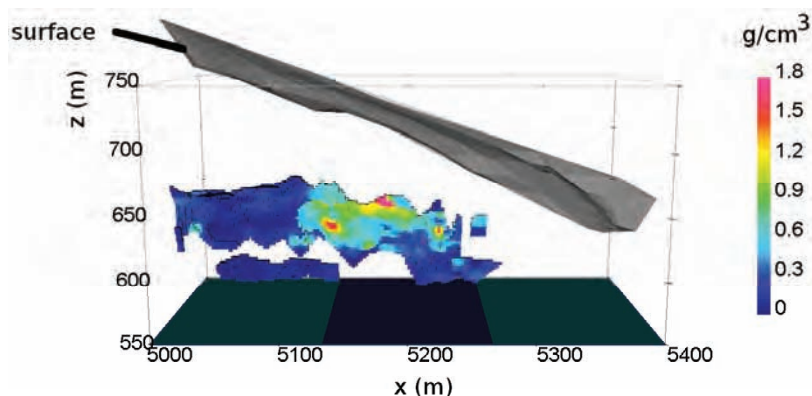

FIG. 3. Model of the anomalous density for the Price massive sulfide deposit, Vancouver Island, Canada, derived from drill core data. The host-rock density (2.7 g/cm³) has been subtracted. The z-axis is measured in meters above sea level. Surface topography is also shown.
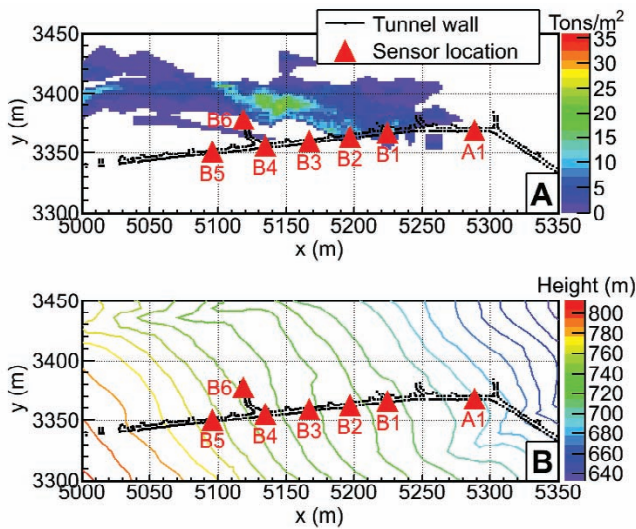
FIG. 5. A. Anomalous mass thickness (in tons per m²) of the Price deposit from drill data, in the X-Y plane, showing the muon sensor locations. The dotted outline is the Price 5 tunnel. B. Topography contours.
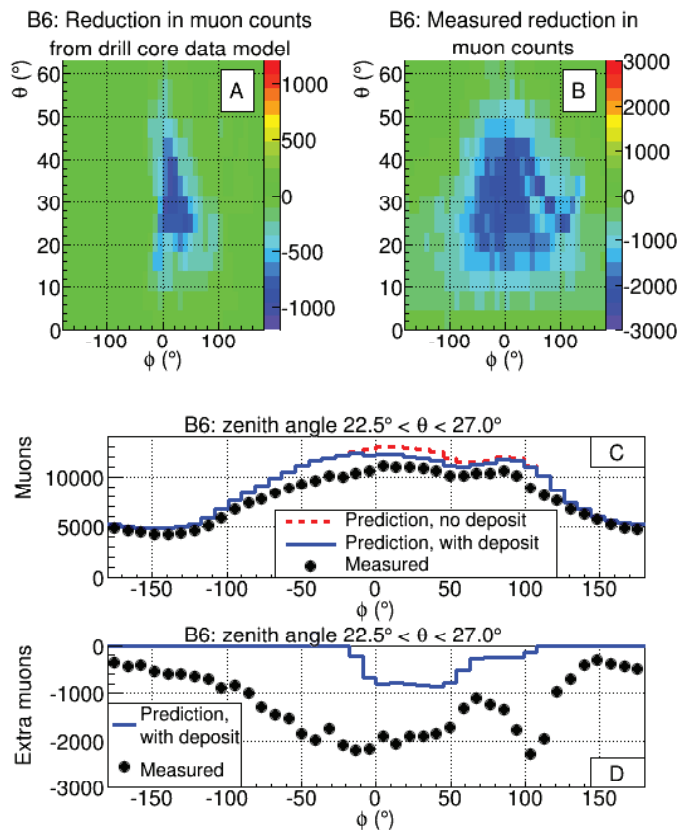
systematically less than the predicted counts over the entire azimuth angle range, which was most likely due to the host-rock density being greater than 2.7 g/cm³, or a small error in the models for calculating underground muon flux, or a combination of these two effects. In addition, Figure 6D shows that the measured anomalous mass signal had two distinct peaks at $\phi \approx -15°$ and $100°$. The peak at $\phi \approx -100°$ was traced to a gully in the mountainous topography that was improperly mapped by the LIDAR survey. The peak at $\phi \approx -15°$ was apparently caused by the presence of anomalous mass.

Before inverting the field data, we forward modeled (simulated) cosmic ray muon data using the drill core data model and the chosen sensor locations, and then carried out an inversion to recover the density distribution. The default cell density value for the inversion was 2.7 g/cm³ but all subsurface cells were unconstrained in the inversion, i.e., cells could take any density value during the inversion.

Volume-rendered 3-D images of the drill core data model and the anomalous density from inverting this model are shown in Figures 7 and 8. In the Z-X plane (Fig. 7) we
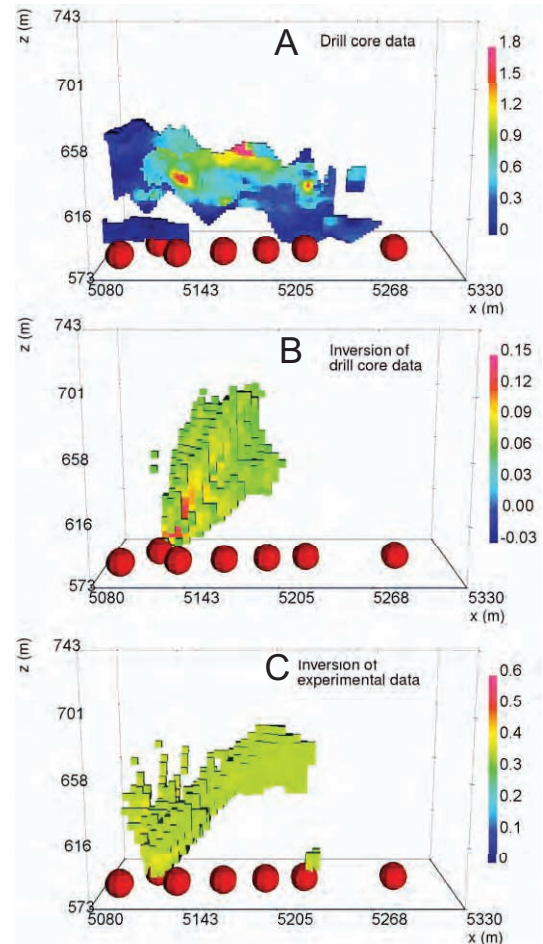

FIG. 6. A. The expected difference of muon counts from a uniform rock density for the B6 sensor location based on the drill core model for each zenith angle (θ) and azimuth angle (ϕ). B. The observed difference in muon counts. C. A region of zenith angle (22.5–27°), showing the expected number of muon counts vs. ϕ from the drill core model and from measured field data. D. The difference in muon counts from a uniform rock density vs. ϕ as predicted from the drill core model and from the measured data for the same zenith angle region as in (C).

FIG. 7. Comparison of 3-D images of anamolous density in the Z-X plane for original drill core data (A), inversion of the synthetic cosmic ray muon data derived from the drill core model (B), and inversion of the experimental cosmic ray muon data (C). Each cell shows the anomalous density (ρ_a) that was defined in equation (6). For the drill data (field data) inversion, cells with $\rho_a < 0.065$ g/cm³ ($\rho_a < 0.35$ g/cm³) are suppressed. The sensor locations are shown as red spheres.
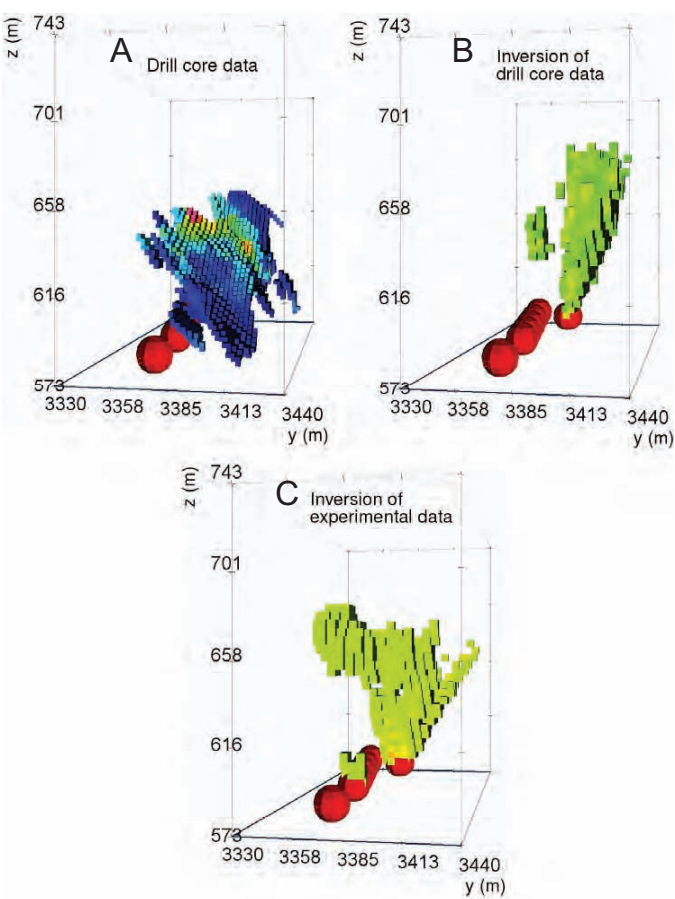
FIG. 8. Comparison of 3-D images of the anomalous density data in the Z-Y plane for original drill core data (A), inversion of the synthetic data derived from the drill core model (B), and inversion of the experimental data (C). Each cell shows the anomalous density (ρ_a) that was defined in equation (6). For the drill data inversion (field data inversion), cells with ρ_a <0.065 g/cm³ (ρ_a < 0.35 g/cm³) are suppressed. The sensor locations are shown as red spheres.

to the orebody resulted in the majority of ray paths crossing the high-density ore zone at small zenith angles. This caused a large solution ambiguity in the vertical direction, resulting in smearing of density values above the known deposit location. Similar distortions are well known in seismic inversions (Bregman et al., 1989).

The smoothing constraint used in equations (3) to (5) resulted in density values that were significantly lower for the inverted image (Fig. 7B) compared to the drill core data (Fig.7A). This was because minimizing the ϕ_m term (eq 3) both promoted smoothness and reduced the length of the model vector $\boldsymbol{\rho}$, leading to solutions with lower average anomalous density.

The cosmic ray muon field data were inverted and the results are included in Figures 7C and 8C. The anomalous density distribution representing the deposit was recovered in approximately the same location as the model derived from drill data and with similar features. The coordinates of the center of mass are calculated in Table 1, where the differences between the simulated and experimental inversions were up to 20 m; this discrepancy was reasonable given that the drill core model was derived from holes spaced at 15- to 30-m intervals. The anomalous density values were systematically larger for the field data compared to the drill data inversion because the field data were incompatible with a host-rock density of 2.7 g/cm³. However, the density contrast sensitivity is not dependent on average host-rock density.

We considered applying other geophysical techniques to survey the Price deposit in order to compare to muon geotomography results. In particular, data from a gravity survey could have been inverted to form a 3-D density image and the data then used in a joint inversion with muon data (Davis et al., 2011). However, a gravity survey was not undertaken because a calculation of the gravity effect from the model (Fig. 3) found a maximum anomaly of just 0.022 mGal from the Price deposit. This would be difficult to detect considering its small magnitude with respect to errors arising from elevation measurements and difficulties with determining accurate terrain corrections.

Conclusion

An inverted 3-D density image of a massive sulfide deposit produced by muon geotomography had good correspondence with a model derived from drill core data. This represents the first controlled test confirming the capability of muon geotomography for imaging a dense orebody in a complex geologic environment. The demonstrated ability to perform accurate forward model simulations makes the sensitivity of the technique predictable for specific survey situations.

Three-dimensional images from muon surveys may be used to guide drilling operations toward regions of high-density

observed that only a portion of the deposit had been recovered by the inversion code (compare Fig. 7A with 7B). This was because the sensor could only measure muons up to a zenith angle of about 60°, and the available mine tunnels prevented us from achieving complete angular coverage. In the Z-Y plane (Fig. 8) the anomalous density reproduced the central section of the original drill data but there were additional distortions, most notably an elongation of density values in the vertical (z) direction. This distortion was not surprising given that all the sensors were located approximately along a straight line determined by the tunnel. The limitations of available locations for the sensors and their positions relative

TABLE 1. Center of Mass Comparison Between the Inversion of Simulated Muon Data Based on Drill Core Data and Inversion of Experimental Data

Center of mass coordinate	Drill data model (m)	Inversion of drill data (m)	Inversion of experimental data (m)	Difference between inversions (m)
X	5,164	5,175	5,196	−21
Y	3,386	3,395	3,380	15
Z	627	648	656	−8

contrast, thereby significantly reducing costs and environmental impact associated with locating and delineating orebodies. The environmental benefits gained from improved imaging include reduced trenching, reduced ore dilution, and improved economic performance of mines. Reduced dilution increases ore grade, reduces the energy expanded in hauling, crushing, and treating waste rock, and further minimizes the volume of tailings.

Muon geotomography produces the most accurate 3-D density distributions when sensors are placed such that they can view the region under study from a range of different angles. In future, borehole sensors will also be developed to provide enhanced capabilities for achieving relatively unrestricted angular ranges for muon geotomography measurements at depths of up to about 1 km.

Acknowledgments

REFERENCES

Alvarez, L.W., Anderson, J.A., El Bedwei, F., Burkhard, J., Fakhry, A., Girgis, A., Goneid, A., Hassan, F., Iversion, D., Lynch, G., Miligy, Z., Moussa, A.H., Sharkawi, M., and Yazolino, L., 1970, Search for hidden chambers in the pyramids: Science, v. 167, p. 832–839.

Beringer, J. et al. (Particle Data Group), 2012, The review of particle physics: Physics Review D, v. 86, 010001.

Bregman, N.D., Bailey, R.C., and Chapman, C.H., 1989, Ghosts in tomography: The effects of poor angular coverage in 2-D seismic traveltime inversion: Canadian Journal of Exploration Geophysics, v. 25, p. 7–27.

Davis, K., Oldenburg, D.W., Kaminski, V., Pilkington, M., Bryman, D., Bueno, J., and Liu, Z., 2011, Joint 3-D inversion of muon tomography and gravity data: Society of Exploration Geophysicists International Workshop on Gravity, Electrical, and Magnetic Methods and Their Applications, Beijing, China, Proceedings, p. 81.

George, E.P., 1955, Cosmic rays measure overburden of tunnel: Commonwealth Engineer, v. 8, p. 455–457.

Golub, G.H., Heath, M., and Wahba, G., 1979, Generalized cross-validation as a method for choosing a good ridge parameter: Technometrics, v. 21, p. 215–223.

Grieder, P.K.F., 2001, Cosmic rays at Earth: Amsterdam, Elsevier Science, 1112 p.

Groom, D.E., Mokhov, N.V., and Striganov, S.I., 2001, Muon stopping power and range tables 10 MeV-100 TeV: Atomic Data and Nuclear Data Tables, v. 78, p. 183–356.

Hamilton, J.V., 1995, Aspects of the geology of Price Hillside and Thelwood Valley, Myra Falls, Vancouver Island: Implications for groundwater hydrology: Report submitted to Geological Survey of Canada and Westmin Resources Ltd., 90 p.

Hansen, P.C., 2000, The L-curve and its use in the numerical treatment of inverse problems, *in* Johnston, P., ed., Computational inverse problems in electrocardiology: Southampton, WIT Press, 289 p.

Juras, S.J., 1987, Geology of the polymetallic volcanogenic Buttle Lake Camp, with emphasis on the Price hillside, central Vancouver Island, British Columbia, Canada: Ph.D. thesis, Vancouver, BC, University of British Columbia, 279 p.

Menke, W., 1989, Geophysical data analysis: Discrete inverse theory: San Diego, Academic Press, 289 p.

MINERvA collaboration, 2006, The MINERvA technical design report (http://minerva-docdb.fnal.gov/cgi-bin/ShowDocument?docid=700).

Muller, J.E. , 1980, The Paleozoic Sicker Group of Vancouver Island, British Columbia: Geological Survey of Canada Paper 79-30, 23 p.

Oldenburg, D.W., and Li, Y., 2005, Geophysical inversion: A tutorial, in Butler, D.K., ed., Society of Exploration Geophysicists Volume in Environmental Geophysics, Investigations in Geophysics no. 13, p. 89–150.

Parker, R.L., 1994, Geophysical inverse theory: Princeton, NJ, Princeton University Press, 400 p.

Tanaka, H.K., Taira, M.H., Uchida, T., Tanaka, M., Takeo, M., Ohminato, T., Aoki, Y., Nishitama, R., Shoji, D., and Tsuiji, H., 2011, Three-dimensional computational axial tomography scan of a volcano with cosmic ray muon radiography: Journal of Geophysical Research, v. 115, p. B12332.

Tang, A., Horton-Smith, G., Kudryavtsev, V.A.., and Tonazzo, A., 2006, Muon simulations for Super-Kamiokande, KamLAND, and CHOOZ: Physical Review D, v. 74, p. 053007.

Tikhonov, A.N., and Arsenin, V.Y., 1977, Solution of ill-posed problems: Washington, D.C., Winston Press, 258 p.